

Invariant embedding approach to secondary electron emission from metals

F. X. Bronold and H. Fehske

Institut für Physik, Universität Greifswald, 17489 Greifswald, Germany

(Dated: January 14, 2022)

Based on an invariant embedding principle for the backscattering function we calculate the electron emission yield for metal surfaces at very low electron impact energies. Solving the embedding equation within a quasi-isotropic approximation and using the effective mass model for the solid, experimental data are fairly well reproduced provided (i) incoherent scattering on ion cores is allowed to contribute to the scattering cascades inside the solid and (ii) the transmission through the surface potential takes into account Bragg gaps due to coherent scattering on crystal planes parallel to the surface as well as randomization of the electron's lateral momentum due to elastic scattering on surface defects. Our results suggest that in order to get secondary electrons out of metals, the large energy loss due to inelastic electron-electron scattering has to be compensated for by incoherent elastic electron-ion core scattering, irrespective of the crystallinity of the sample.

I. INTRODUCTION

Secondary electron emission upon electron impact has been investigated ever since the start of modern solid state physics [1]. It is at the core of many technological applications, for good and for bad, ranging from surface analysis [2, 3] over materials processing [4] and electron storage rings, where electron multipacting due to secondary electrons may limit the ring's performance [5], to various plasma devices [6–13]. Hence, a great number of experimental and theoretical work has been done in this field (for references to recent work see, for instance, the surveys in [14, 15]). Most of it is concerned with electron emission due to primary electrons hitting the surfaces at high energies, above 100 eV [15]. In plasma devices, however, which are our main interest, the primaries triggering secondary electrons typically have energies below 50 eV. For instance, in dc microdischarges [11], the electron distribution functions close to the electrodes have substantial weight below 50 eV. Most of the electrons hitting the walls confining the plasma have thus energies in a range where collective phenomena of the solid, such as diffraction, the surface potential, and polarization effects, start to play a role.

The purpose of this work is to present an approach for calculating the emission yield which accounts for these phenomena and to apply it to metal surfaces at very low electron impact energies. Instead of using kinetic equations of the Boltzmann-type [16, 17] or Monte-Carlo simulations of the process [18–21], we employ the invariant embedding principle. Originally developed by Ambartsumian [22] and Chandrasekhar [23] for the description of radiative transport in stellar atmospheres, Dashen [24] has shown quite some time ago that it can be also used to analyze electron backscattering from solid surfaces. Various groups pursued since then the principle [25–30]. But its full potential has not been tapped yet because the applications were either restricted to elastic scattering or to radiative transfer.

In previous studies, we employed the principle to calculate the sticking [31] and reflection [32] probabilities for an electron hitting a dielectric surface. To avoid electron-

electron scattering, leading to electron multiplication due to the two final states, we restricted however the considerations to impact energies below the band gap. By adopting the reasoning of Wolff [16], later refined by Penn and coworkers [17], we now enable our approach to treat also electron-electron scattering.

Besides generalizing conceptually our previous approach, we also develop in this work a numerical scheme, based on a quasi-isotropic approximation for the angular integrals, which solves the nonlinear embedding equation for the electron backscattering function (and not just its linearization [31, 32]), while keeping the scattering processes inelastic as well as angle-dependent. Analyzing within this scheme experimental data for various metals, we also hope to clarify two issues, raised specifically by Cimino and coworkers' experiments on clean and as-received noble metal surfaces [5, 33, 34], which led in the plasma physics community to a debated [35, 36] revival of interest in low-energy electron backscattering from surfaces: (i) The discrepancy between the recent [5, 33, 34] and previous measurements by Bronshtein and Roshchin [37] and (ii) the increase of the emission yields to unity for vanishing impact energy found in the recent data.

Using an effective mass model, augmented by electron scattering on the ion cores, Bragg diffraction on the crystal planes parallel to the surface, and scattering on surface defects, we find rather good agreement with measured data [34, 37–42]. Except for the scattering strength of the surface defects, the model contains no free parameters. From a broader perspective, our results suggest (i) that electron-electron scattering alone yields essentially no secondary electrons, the emission yields being given in that case by the electron reflectivities of the metal surfaces, which, in the absence of Bragg gaps, are very small due to the image charge effect, (ii) the potentials of the ion cores act as incoherent scattering centers, irrespective of the crystallinity of the sample, implying that Bauer's radium model [43], often used at high impact energies, may be a better starting point for the theoretical analysis of low energy data as one would perhaps expect, and (iii) inclusion of surface imperfections in the

surface transmission function may be also required for a quantitative description of electron emission at very low impact energies.

The outline of the paper is as follows. In Section II we present our approach. It is divided into three subsections, introducing the expression for the emission yield, the definition of the backscattering function together with its determination via the embedding equation, and the augmented effective mass model for the solid. Section III presents numerical results for Al, W, and the noble metals Cu, Ag, and Au. Concluding remarks are given in Section IV while technical details interrupting the flow of the presentation are given in three appendices.

II. CALCULATIONAL APPROACH

A. Electron emission yield

To calculate the electron emission yield due to a primary electron hitting the metal surface with an energy E and an external direction cosine $\xi = \cos \beta$, we image the electron to first encounter the surface potential of depth $U = E_F + \Phi$, where E_F and Φ are the Fermi energy and work function of the metal. For an idealized surface, with perfect homogeneity in the lateral directions, the azimuth angles can be integrated out. Only the polar angles thus enter the formalism, giving rise to the direction cosines. In case the electron successfully traverses the potential, it may initiate scattering cascades inside the metal leading to electrons which in turn may escape the solid if they are directed towards the interface and have enough kinetic energy in the perpendicular motion to traverse the surface potential from the inside out.

The emission yield $Y(E, \xi)$ may thus be expressed as (throughout we measure energy in Rydbergs, length in Bohr radii, and mass in bare electron masses)

$$Y(E, \xi) = R(E, \xi) + (1 - R(E, \xi))\mathcal{E}(E, \xi), \quad (1)$$

where $R(E, \xi)$ is the reflection probability due to the metal's surface potential and

$$\mathcal{E}(E, \xi) = \int_{\eta_{\min}(E)}^1 d\eta' \int_{E_{\min}(\eta')}^E dE' \rho(E') \mathcal{B}(E\eta(\xi)|E'\eta') D(E', \xi(\eta')) \quad (2)$$

is the escape function, describing the emission of secondary electrons due to the scattering cascades inside the metal. It contains the density of states $\rho(E)$ of the metal's conduction band, the transmission probability

$$D(E, \xi) = 1 - R(E, \xi), \quad (3)$$

and the function $\mathcal{B}(E\eta|E'\eta')$, encoding backscattering cascades from an initial electron state (E, η) to a final electron state (E', η') . The functions $\xi(\eta)$ and $\eta(\xi)$ connect internal and external direction cosines and are im-

plicitly defined by the relation

$$1 - \eta^2 = (1 - \xi^2) \frac{E}{E + U}, \quad (4)$$

where we assumed (as for all formulae presented below) a quadratic dispersion for the conduction band of the metal, with an effective mass equal to the bare electron mass. The relation follows from the conservation of energy and lateral momentum at the interface. Constraining the integrations over η' and E' from below by $\eta_{\min}(E) = \sqrt{U/(E+U)}$ and $E_{\min}(\eta') = U(1/\eta'^2 - 1)$ ensures that only backscattered electrons with a perpendicular kinetic energy larger than the depth of the surface potential contribute to the emission yield. For the quadratic dispersion, finally, $\rho(E) = \sqrt{(E+U)}/2$.

The scattering geometry and the structure of Eqs. (1) and (2) are visualized in Fig. 1a. From it, the definition of the direction cosines can be also inferred, $\eta' = |\cos \theta'|$ with $\pi/2 \leq \theta' \leq \pi$ and $\eta = \cos \theta$ with $0 \leq \theta \leq \pi/2$. Similar relations hold for the external direction cosines ξ and ξ' and their corresponding angles. The surface potential we use for the calculation of the transmission function $D(E, \xi)$ is also indicated. In addition to the image tail, we allow for Bragg scattering on crystal planes parallel to the interface. Before we describe how we calculate the functions entering our approach, we generalize it to an imperfect interface, where electrons may scatter elastically on surface defects while passing the interface.

At an imperfect surface, lateral momentum is not conserved due to lack of in-plane homogeneity. To take this possibility into account we employ an approach which was originally developed by Smith and coworkers [44] to analyze ballistic electron spectroscopy data for semiconductor-metal interfaces. Later, we used it to study the interaction of an electron with imperfect dielectric surfaces [31, 32]. Adopting the notation to the case of metals, the emission yield for an imperfect metal surface becomes,

$$\bar{Y}(E, \xi) = 1 - \bar{S}(E, \xi), \quad (5)$$

where

$$\begin{aligned} \bar{S}(E, \xi) &= \frac{D(E, \xi)}{1 + C/\xi} [1 - \bar{\mathcal{E}}(E, \xi)] \\ &+ \frac{C/\xi}{1 + C/\xi} \int_0^1 d\xi' D(E, \xi') [1 - \bar{\mathcal{E}}(E, \xi')] \end{aligned} \quad (6)$$

is the probability (strictly speaking, quasi-probability, see next subsection) for not emitting an electron. The function $\bar{\mathcal{E}}(E, \xi)$ entering this expression is given by (2) with $D(E, \xi)$ in the integrand replaced by

$$\bar{D}(E, \xi) = \frac{D(E, \xi)}{1 + C/\xi} + \frac{C/\xi}{1 + C/\xi} \int_0^1 d\xi' D(E, \xi'). \quad (7)$$

The function $\bar{D}(E, \xi)$ describes the transmission through the surface potential in the presence of elastic

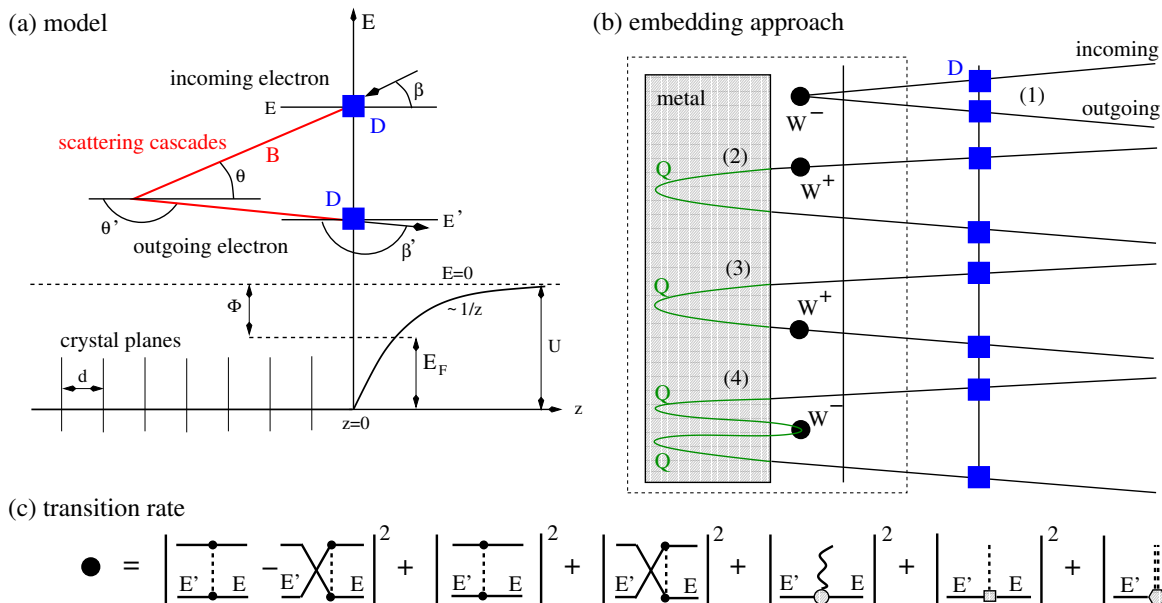


FIG. 1. (color online) (a) Illustration of the main parts of the surface model. (b) Principle of invariant embedding as used to determine the function $\mathcal{B}(E\eta|E'\eta')$ into which the scattering cascades are encoded and (c) diagrammatic representation of the processes included in the transition rate $W^\pm(E\eta|E'\eta')$. The first three terms are due to electron-electron scattering, while the following ones are due to electron-phonon, electron-impurity, and electron-ion core scattering. The labelling of the diagrams is not complete. It is only meant to indicate where in the diagrams the initial and final states appear.

scattering on defects. It causes relaxation of the lateral momentum. Diffuse transmission (second term in (7)) is thus possible at expense of ballistic transmission (first term in (7)). The scattering strength C is proportional to the product of the absolute square of the matrix element and the defect concentration. Both are unknown. We thus take C as an adjustable parameter. The emission yield of the perfect surface, Eq. (1), is recovered from Eqs. (5)–(7) in the weak scattering limit $C \ll 1$, while the yield of a rather dirty, irregular surface is given in the strong scattering limit $C \gg 1$.

B. Backscattering function

The scattering cascades inside the metal are encoded in the function $\mathcal{B}(E\eta|E'\eta')$, which in turn is related to the backscattering function $Q(E\eta|E'\eta')$ which, following the work of Dashen [24], is obtained from the invariant embedding principle depicted in Fig. 1b. The principle states that adding an infinitesimally thin layer of the same material to a halfspace already filled by it does not change the backscattering. It leads to the embedding equation for $Q(E\eta|E'\eta')$. Decoupling angle and energy variables by the quasi-isotropic approximation described in Appendix A, the embedding equation reads

$$\begin{aligned}
 Q(E|E'; \eta\eta') &= K^-(E\eta|E'\eta') + \int_{E'}^E dE'' K_1^+(E|E''; E'\eta\eta') Q(E''|E'; \eta\eta') + \int_{E'}^E dE'' Q(E|E''; \eta\eta') K_2^+(E''|E'; E\eta\eta') \\
 &+ \int_{E'}^E dE'' \int_{E'}^{E''} dE''' Q(E|E''; \eta\eta') B^-(E''|E'''; E E'\eta\eta') Q(E'''|E'; \eta\eta'), \quad (8)
 \end{aligned}$$

where the notation $Q(E|E'; \eta\eta')$ signals the different status of the energy and angle variables, with only the former affected by the integrations and the latter simply external parameters.

The validity of the decoupling hinges on the angular dependence of $K^-(E\eta|E'\eta')$. It should be nearly isotropic. In this sense, the decoupling is closely related

to the transport approximation employed by Werner and coworkers in their analysis of elastic electron backscattering from surfaces [45]. Using the surface model described in the next subsection, we show in Appendix A data for $K^-(E\eta|E'\eta')$ which suggest that, for elastic scattering the approximation is indeed well justified, while for inelastic electron-electron collisions it becomes some-

what questionable, especially for large direction cosines. However, the rather good agreement between calculated and measured emission yields supports—in retrospect—the assumption that, as a first step towards solving the full embedding equation, the angular dependence of $K^-(E\eta|E'\eta')$ can be considered nearly isotropic, irrespective of the energy transfer. Details of the decoupling and the definition of the functions K^- , K_1^+ , K_2^+ , and B^- are given in Appendix A.

Separating inelastic electron-electron from elastic collisions by writing the functions entering Eq. (8) as a sum of two terms,

$$A(E|E'; \eta\eta') = A_{ee}(E|E'; \eta\eta') + A_{el}(E; \eta\eta')\delta(E - E'), \quad (9)$$

and expanding the inelastic part of the backscattering function in the number of backscattering events,

$$Q(E|E'; \eta\eta') = \sum_{l=0}^{n_{\max}} Q_{ee}^{(2l+1)}(E|E'; \eta\eta') + Q_{el}(E; \eta\eta')\delta(E - E'), \quad (10)$$

enables us to solve the embedding equation by an iterative process which successively increases the number of inelastic backscattering events. The functions $Q_{ee}^{(2l+1)}(E|E'; \eta\eta')$ turn out to satisfy a set of linear integral equations with kernels renormalized by $Q_{el}(E; \eta\eta')$, which itself is given by the positive solution of a quadratic algebraic equation. Essential for the feasibility of the approach is the Volterra-type structure of the energy integrals in the embedding equation. It allows to sweep the EE' -plane in such a manner that the $Q_{ee}^{(k)}$ appearing in the kernels of the integral equation for $Q_{ee}^{(n)}$ with $n > k$ are given from the previous steps. The renormalized kernels and further details about our strategy to solve (8) are given in Appendix B.

To obtain the function $\mathcal{B}(E\eta|E'\eta')$ entering (2), we have to keep in mind that not all backscattered electrons leave the solid. We also have to take into account that in an electron-electron scattering event, the initial electron leads to two final electrons. In terms of the two contributions to the backscattering function, Q_{ee} and Q_{el} , we therefore write

$$\mathcal{B}(E\eta|E'\eta') = \frac{2Q_{ee}(E|E'; \eta\eta') + Q_{el}(E'; \eta\eta')\delta(E - E')}{\int_{-\Phi}^E dE'' \int_{\eta_c}^1 d\eta'' \rho(E'')Q(E|E''; \eta\eta'')}, \quad (11)$$

where the factor two in front of Q_{ee} in the numerator accounts for the two final electrons in an electron-electron backscattering event [16, 17] and the normalization ensures that—at the end in Eq. (2)—only backscattered electrons contribute to the emission yield which make it also over the potential barrier and thus leave the metal. Hence, with the function $\mathcal{B}(E\eta|E'\eta')$ defined in (11), the escape function (2) formally resembles a conditional (pseudo-)probability (without electron-electron collisions, that is, without electron multiplication, it would be a probability in the strict sense).

The treatment so far did not use any properties of the transition rates associated with the elementary scattering processes. Only the angular dependencies are postulated to behave in a manner to justify the decoupling of the energy and angle variables. To furnish the equations, a model for the solid is required.

C. Augmented effective mass model

To obtain numerical results we need a model for the surface potential and a model for the bulk scattering processes. The former enters the calculation of the transmission function $D(E, \xi)$, while the latter is required for the kernels of the embedding equation, from which $Q(E|E'; \eta\eta')$ and subsequently $\mathcal{B}(E\eta|E'\eta')$ follow.

Keeping the model flexible and transparent, we use an augmented effective mass model, requiring only a few readily accessible material parameters. The simplest model of this kind for the surface potential is an image step as shown in Fig. 1a. To also account for energy gaps in the transmission function $D(E, \xi)$, we follow García and Solana [46] and augment the potential on the solid side, that is, for $z < 0$ by a potential $V(z)$ periodic in z . Using also results from MacColl [47], the reflection probability in the two-band approximation is then given by

$$R(E, \xi) = \left| \frac{\sqrt{\tilde{E}_z} - \sqrt{E_z} y + C_{\pm} [\sqrt{\tilde{E}_z} - \sqrt{E_z} y - G]}{\sqrt{\tilde{E}_z} + \sqrt{E_z} y^* + C_{\pm} [\sqrt{\tilde{E}_z} + \sqrt{E_z} y^* - G]} \right|^2 \quad (12)$$

with $E_z = E\xi^2$, $\tilde{E}_z = E_z + U$, and

$$y = -2W'_{-i/4\sqrt{E_z}, 1/2}(i\sqrt{E_z}/U)/W_{-i/4\sqrt{E_z}, 1/2}(i\sqrt{E_z}/U), \quad (13)$$

where $W_{k,\lambda}(z)$ are Whittaker functions and $()'$ denotes the derivative with respect to the argument of the function. Using relations between Whittaker functions and their derivatives, the ratio y can be expressed as a continued fraction [48] and determined numerically. The parameter

$$C_{\pm} = \frac{E_{\pm}(G/2) - E_0(G/2)}{V_G}, \quad (14)$$

with $E_0(G/2) = (G/2)^2 - U$ and $E_{\pm}(G/2) = E_0(G/2) \pm V(G)$, contains the information about the Bragg gap, which forms—within the two-band model—at wave number $k = G/2$. It can be verified by inspection that $R(E, \xi) = 1$ for $C = \pm 1$, leading to total reflection for energies inside the gap. The model for the Bragg gap can be used in two ways. Either one calculates V_G from the Fourier transform of the pseudopotential of the ion cores, setting $G = 2\pi n_B/d$, where d is the spacing between the lattice planes and n_B is the order of the Bragg gap, or one uses it as an effective model, identifying $E_+(G/2)$

and $E_-(G/2)$ with the experimentally found upper and lower edges of the gap, E_U and E_L , respectively. In that case, $V_G = (E_U - E_L)/2$. In this work we pursue only the second approach.

In the bulk, we include inelastic scattering between electrons and elastic scattering on impurities, phonons, and ion cores. Phonon scattering is thus described in the quasi-elastic approximation. The scattering on the ion cores is included without an energy threshold, although one would perhaps expect it to be operative only at much higher energies [49]. However, even an electron approaching the surface with vanishing impact energy has, after traversing the metal's surface potential, an energy in the conduction band which is equal to the depth U of the potential. For the metals considered, the corresponding de Broglie wave length turns out to be on the order of the lattice spacing. Since, in addition, electrons are scattered in arbitrary directions, not only in high-symmetry directions, secondary electrons may be affected by the ion cores. Indeed, we found it essential to include this scattering process to get numerical results in agreement with experimental data. The model we use for the bulk is thus essentially the randium model of Bauer [43].

The transition rate resulting from the scattering processes listed above is visualized in Fig. 1c. It is the sum of the Fermi Golden Rule rates for the individual processes. Expressing electron momenta in terms of total energies, direction cosines, and azimuth angles (spherical coordinates in momentum space with the outward directed surface normal as the z -axis), and distinguishing between forward and backward scattering, depending on the sign of the z -components of the electron momenta, yields the expressions we now give without calculation.

The rate due to elastic scattering processes becomes

$$W_{el}^{\pm}(E\eta|E'\eta') = 16n_e \left[(x_{imp} + 3\frac{k_B T}{E_F}\lambda) \langle V(g^{\pm}, 0)^2 \rangle_{\phi} + Z_v \langle V(g^{\pm}, \alpha_c)^2 \rangle_{\phi} \right] \delta(E - E') \quad (15)$$

with the momentum transfer

$$g^{\pm} = |\vec{k} - \vec{k}'|^{\pm} = g^{\pm}(E\eta|E'\eta'; \phi) \quad (16)$$

written in terms of total energies, direction cosines, and the difference of the azimuth angles, which in Eq. (15) is integrated over according to $\langle (\dots) \rangle_{\phi} = \int_0^{2\pi} d\phi (\dots)$. The parameters n_e , x_{imp} , λ , and Z_v denote, respectively, the electron density of the metal, the impurity concentration in units of n_e , the electron-phonon coupling parameter, and the valence of the ion cores. The function

$$V(q, \alpha_c) = \frac{1}{q^2 + \kappa^2} \left(1 - \frac{\alpha_c}{8\pi Z_v} \frac{q^2}{(1 + (qr_c)^2)^2} \right) \quad (17)$$

becomes for $\alpha_c \neq 0$ Harrison's empirical ion pseudopotential [50] while for $\alpha_c = 0$ it reduces to the Hückel potential with the screening wave number κ of a degenerate electron gas at room temperature and density n_e .

The rate for electron-electron scattering contains direct and exchange terms. In terms of the variables we use, the exchange terms force the expression for the rate to be rather clumsy. For the moment, we thus give only the rate due to the direct terms,

$$W_{ee}^{\pm}(E\eta|E'\eta')|_D = \langle V(g^{\pm}, 0)^2 N(g^{\pm}, E' - E) \rangle_{\phi} \quad (18)$$

with $V(q, \alpha_c)$ given by (17) and

$$N(q, \omega) = \frac{1}{q\pi^2} \int_{\varepsilon_{\min}(q, \omega)}^{\infty} d\varepsilon n_F(\varepsilon + \omega) [1 - n_F(\varepsilon)] , \quad (19)$$

where $\varepsilon_{\min}(q, \omega) = (\omega - q^2)^2/4q^2$ and $n_F(\varepsilon)$ is the Fermi function for the conduction band electrons. The full transition rate, W_{ee}^{\pm} , including the exchange terms, is however used to produce the data shown in Section III. It is given in Appendix C.

The connection of the transition rates to the kernels of the embedding equation can be found in Appendix A. With the material parameters given in Table I we have everything together to calculate the emission yields for the metals listed. Our approach is geared towards low impact energies, where solid state effects become important. Electron emission caused by high energy electrons is not addressed.

III. RESULTS

We now present calculated emission yields for different metal surfaces and compare them to measured data. The material parameters for the metals are summarized in Table I. Electron-electron exchange scattering is included, although the Monte-Carlo integration it requires increases the computational time by two orders of magnitude. Depending on energy and sample, it may change, however, the yields up to twenty percent and can thus not be excluded. A few remarks about the parameters of the numerics are given in Appendix B. In the plots shown below, energies are always measured from the potential just outside the metal (vacuum level).

We start with the emission yield for aluminum shown in Fig. 2. Since the experimental data by Bronshtein and Roshchin [37] (as given by Andronov [36]) are for polycrystalline aluminum, we do not include Bragg scattering on crystal planes parallel to the surface in the calculation. We also expect the lateral momentum not to be conserved due to surface defects. Indeed, for $C = 10$ we obtain better agreement with the measured data than for $C = 0$. For the ion pseudopotential (17) we employed a plain Hückel potential ($\alpha_c = 0$) because our calculational scheme turned out to be unstable for the Al parameters given by Harrison [50]. Besides the humps around 5 eV and 10 eV, whose origin has to be sought most probably in details of the surface's electronic structure beyond the simple two-band model we employ for the calculation of the surface transmission function, the theoretical

	$d[\text{\AA}]$	$\Phi[\text{eV}]$	$E_F[\text{eV}]$	λ	x_{imp}	Z_v	α_c	r_c
Au	4	5.3	5.5	0.08	0.01	1	83.34	0.313
Ag	4	4.4	5.5	0.12	0.01	1	69.0	0.457
Cu	3.6	4.7	7.0	0.16	0.01	1	59.1	0.516
Al	4	4.25	11.7	0.42	0.01	3	0.0	–
W	3.16	5.22	6.4	0.28	0.01	2	0.0	–

TABLE I. Lattice constant d , work function Φ , Fermi energy E_F , electron-phonon coupling constant λ , impurity concentration x_{imp} in units of the electron density, valence Z_v , and pseudopotential parameters α_c and r_c from [50–52]. If not noted otherwise the parameters are in atomic units, with energy measured in units of Rydbergs, length in Bohr radii, and mass in bare electron masses. The values are typical ones from textbooks [53].

yields are rather close to the experimental data. The augmented effective mass model and the approximate calculation of the backscattering function Q seem thus to capture the essential physics behind secondary emission from polycrystalline Al quite well.

Also shown in Fig. 2 is the emission yield obtained by keeping only electron-impurity and electron-phonon scattering as (quasi-)elastic processes competing with the energy loss due to inelastic electron-electron scattering. As can be seen, even for an impurity concentration $x_{\text{imp}} = 0.01$, that is, for one impurity every 100 electrons, which is rather high, the calculated yield remains way below the measured data. It would require a concentration of the order unity, that is, one impurity for every electron, to bring the theoretical yields up to the measured values. The only elastic scattering process which brings in such a large factor is the scattering of electrons on the potentials of the ion cores. Its rate is proportional to $n_a Z_v^2$, with n_a the atomic density of the solid and Z_v the valence of the atoms inside the solid. Due to charge neutrality, $n_a Z_v = n_e$. Hence, the rate is proportional to $n_e Z_v$. Since Z_v is of the order unity, we have a process which brings in roughly a scattering center for every electron, as required. Without the scattering on the ion cores, the yield is essentially identical to the reflectivity of the image step, which is also plotted in Fig. 2.

For vanishing impact energy the calculated and measured yields do not agree too well. The discrepancy could be remedied by increasing the depth of the surface potential. From MacColl’s calculation [47], however, we infer that the depth $U = \Phi + E_F$ should be more than 20 eV (instead of 15.95 eV we use) to push the reflectivity at zero energy up to the experimental value. Without surface chemistry, for instance, the formation of an oxide layer, which is beyond the scope of the present investigation, it is hard to envisage a solid state effect which could increase the potential depth by such a huge amount. Hence, we did not adjust U to improve the agreement between experimental and theoretical yields further.

The data plotted in Fig. 2 indicate clearly that the

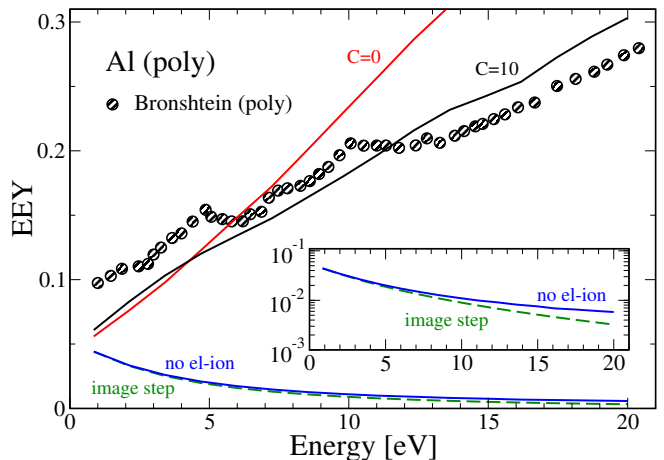


FIG. 2. (color online) Emission yield $Y(E, \xi = 1)$ due to an electron hitting perpendicularly a polycrystalline Al surface with energy E . Measured data are from Bronshtein and Roshchin [37]. Numerical results are shown for an idealized perfect surface ($C = 0$) and a strongly disordered surface ($C = 10$). For comparison, the yields without incoherent scattering on the ion cores and a collisionless image step are also plotted. The inset shows them on a log scale for better visibility.

scattering cascades inside the solid cause secondary emission. This is of course general wisdom and in fact the basis of all theoretical descriptions, including ours. What is surprising, at least to us, is that electron-electron scattering alone yields essentially no emission and that incoherent scattering on the ion cores has to be included. The unexpected necessity to make the ion cores visible to the electrons partaking in the scattering cascades arises however from the fact that once inside the solid, the electron has a kinetic energy of at least the depth U of the surface potential. For Al, $U = 15.95$ eV, leading to a de Broglie wave length $\lambda_{\text{dB}} = 3.1 \text{ \AA}$, which is on the order of the lattice spacing $d = 4 \text{ \AA}$. Since, in addition, not only high-symmetry directions are involved in the scattering cascades, the scattering on the ion cores should play a role in secondary electron emission, irrespective of the crystallinity of the sample.

To understand the vanishing emission yield due to electron-electron scattering, we take a closer look at the transition rates. Figure 3 plots on the left and right, respectively, $W^-(E\eta|E'\eta')$ and $W^+(E\eta|E'\eta')$ for $\eta = 1$ and $\eta' = 0.3$. The top (bottom) row shows the rates without (with) the elastic scattering on the ion cores taken into account. To make the most probable final states of the scattering event identifiable, we normalized the respective rates to their largest values. Clearly, excluding the scattering on the ion cores, a backscattered electron very unlikely finds itself in a final state above the vacuum level. The most probable states are below it, close to the Fermi energy. The same holds for forward scattering. Hence, regardless of the scattering direction, due to the strong energy loss in an electron-electron colli-

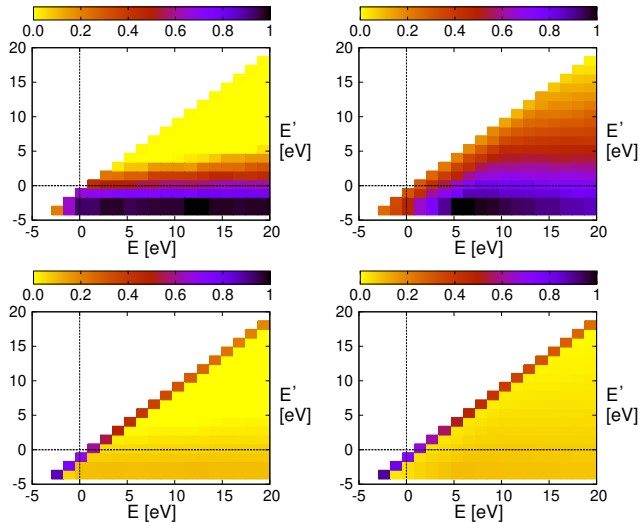


FIG. 3. (color online) Transition rates for Al using the model described in Section II C. Left and right panels display $W^-(E\eta|E'\eta')$ and $W^+(E\eta|E'\eta')$ without (top) and with (bottom) incoherent scattering on ion cores included. The data are normalized to the largest value of the respective transition rates to indicate the most probable final states more clearly. The direction cosines are $\eta = 1$ and $\eta' = 0.3$ (for other values of η' , the plots look qualitatively similar) and the energy resolution $\Delta E \approx 0.7\text{eV}$ is the one taken for the numerical solution of the embedding equation (8) as described in Appendix B.

sion, electrons in the final states will hardly make it over the potential barrier. Including the scattering on the ion cores, in contrast, makes elastically backscattered final states above the vacuum level accessible, as can be seen in the plots of the bottom row. Due to the Volterra-type structure of Eq. (8), this is most favorable for electron emission. Hence, a sizeable emission yield can now be expected.

The scattering on the ion cores makes elastic final states in forward direction also more likely. However, the gain in backscattering above the vacuum level compensates for this detrimental effect. Since the large energy transfer due to electron-electron scattering is a general feature of hot electrons in metals, as can be inferred from the work of Ladstädter and coworkers [54], we suspect, for a secondary electron to get out of a metal, it has to suffer along its way inside the solid also incoherent elastic scattering on the ion cores, irrespective of the metal's crystallinity. Our results for other metals to which we now turn support this conclusion.

To test our approach for metal surfaces with a Bragg gap in the energy range of interest, we consider tungsten (110), (100), and (111) surfaces. The upper and lower edges of the gaps, $E_U = E_+(G/2)$ and $E_L = E_-(G/2)$ in our notation, have been determined experimentally by Willis [55] and can thus be inserted into our formalism as described in the previous section. The remaining parameters for W are given in Table I. Figure 4 plots the

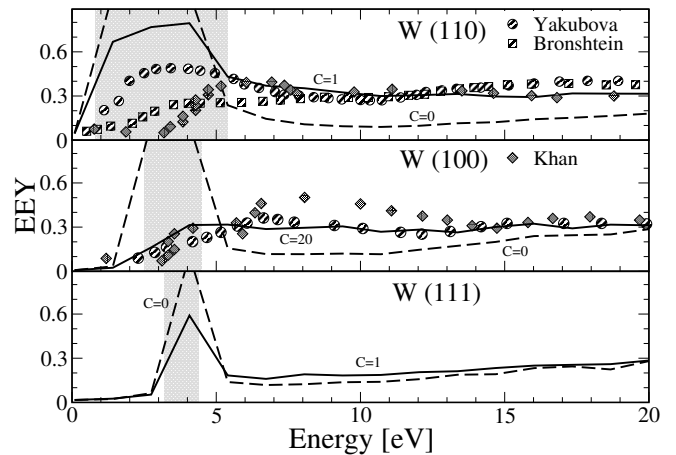


FIG. 4. Secondary emission yield $Y(E, \xi = 1)$ for different single-crystal tungsten surfaces. Experimental data are from Khan and coworkers [42], Bronshtein and Fraiman [41], and Yakubova and Gorbatiyi [39, 40]. Shaded regions indicate Bragg gaps in the electronic structure of the surfaces [55]. The surface parameter C is attached to the theoretical data.

emission yields again for perpendicular impact as a function of energy. The Bragg gaps are the regions shaded in grey and measured data are from Yakubova and Gorbatiyi [39, 40], Khan and coworkers [42], and Bronshtein and Fraiman [41] (as given by Tolias [56]).

Let us start with the data for the W(110) surface, shown in the upper panel of Fig 4. For impact energies larger than the energy gap the experimental data coincide rather well with each other and also with the theoretical yield we obtained by setting the surface defect scattering strength $C = 1$. In the gap region, however, experimental results scatter significantly. Whereas the data from Bronshtein and Fraiman [41] as well as Khan and coworker [42] vanish more or less monotonously with decreasing energy, the data from Yakubova and Gorbatiyi [40] show a hump. We interpret the hump to be due reminiscent to the Bragg gap. With the parameter C we have control over the emission yield in the gap region. For $C = 0$ (dashed line), that is, without interfacial scattering, for an ideal surface, the yield in this region would be unity. The deviation of the experimental data from unity signals the presence of surface defects. Since they couple electron states with different lateral momenta, total reflection cannot be maintained over the gap region. With increasing scattering strength C , the reflectivity reduces thus to less than unity. A reasonable overall fit to the data of Yakubova and Gorbatiyi [40] we obtained for $C = 1$, although in the gap region the theoretical yields are still about a factor two too large.

Emission yields for the (100) and (111) tungsten surfaces are shown, respectively, in the middle and lower panels of Fig. 4. For the latter we could not find experimental data. The theoretical results are thus predictions. On a finer energy grid, the gap region would be better resolved, but the expected increase of the emission yield

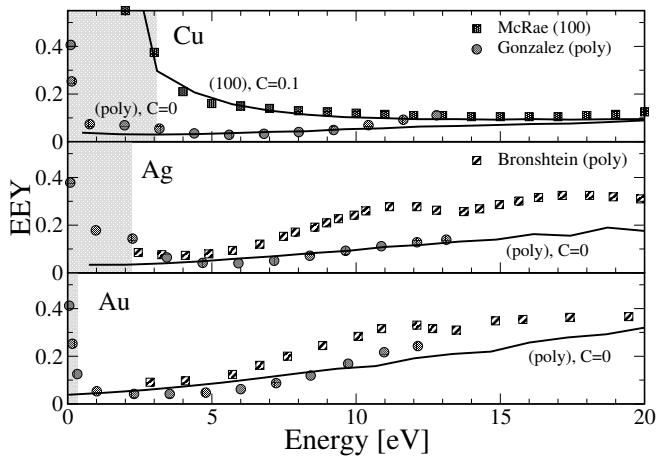


FIG. 5. Secondary emission yield $Y(E, \xi = 1)$ for different noble metal surfaces. Measured data for Cu(100) are from McRae and Caldwell [38], while the data for the polycrystalline Cu, Ag, and Au surfaces are from Gonzalez and coworkers [34] and Bronshtein and Roshchin [37] as indicated. The scattering strength C of the surface defects for which good agreement between theoretical and measured data is obtained are also given in the plot. For reference, the shaded regions indicate the Bragg gaps of the (100) surfaces [57].

can be already seen from the presented data. As far as the (100) surface is concerned, the experimental data from Khan and coworkers [42] and Yakubova and Gorbatiy [39] show no hump in the gap region. The surfaces must have been thus rather disordered to prevent total reflection. Indeed, setting $C = 20$, we reproduce sufficiently well the measured yields. The fair agreement between theory and experiment we reach also for tungsten is a further indication of the viability of our approach. Let us stress that our assumption of incoherent scattering on ion cores contributing also in single crystals to the scattering cascades responsible for secondary emission could be tested by measuring the yields for high-quality, defect-free single-crystal surfaces. If the measured data turn out to be below the dashed lines shown in the three panels of Fig. 4, scattering on ion cores does not contribute and our assumption would be false.

A comparison of calculated yields for the noble metals Cu, Ag, and Au and measured data by Gonzalez and coworkers [34] as well as Bronshtein and Roshchin [37] (as given by Andronov [36]) is shown in Fig. 5. Avoiding a discussion of chemical modifications of the as-received surfaces, which are outside the scope of our approach, we focus on what Gonzalez and coworkers call clean samples. For Cu, we also include data from McRae and Caldwell [38] because they were taken for a single crystal (100) surface, showing a Bragg gap, whereas the other data are for polycrystalline samples, where no Bragg gaps are expected. The grey regions in the three panels indicate, for purpose of reference, the gaps for Cu(100), Ag(100), and Au(100) as obtained from the calculations of Chulkov and coworkers [57].

In the upper panel we see for Cu(100) almost perfect agreement between experiment and theory by setting $C = 0.1$. The surface used by McRae and Caldwell [38] must have been thus nearly void of defects. As far as the polycrystalline Cu employed by Gonzalez and coworkers [34] is concerned, we get fair agreement by excluding the possibility of a Bragg gap and setting $C = 0$, implying a clean surface. Since the surface was indeed carefully cleaned by sputtering with Ar^+ ions, $C = 0$ is perhaps expected. The same we find for the polycrystalline, sputter-cleaned Ag and Au surfaces. As can be seen in the middle and lower panels of Fig. 5, fair agreement between measured and calculated data is again obtained for $C = 0$, although not as good as for Cu.

We could not reproduce Bronshtein and Roshchin's data [37] for Ag and Au, which are for all energies roughly a factor two above the ones measured by Gonzalez and coworkers [34]. The origin of the enhancement remains unclear. Perhaps the surfaces were contaminated by adatoms or oxide layers, but this is outside the scope of the present investigation. Within our model, we have also no explanation for the humps around 11 eV, which in fact do also not show up in the recent data from Gonzalez and coworkers [34]. Since we do not expect plasmon effects to affect backscattering in this energy range, the cause of the humps should be also sought in a chemical modification of the surfaces. Further studies, ideally based on the solution of the embedding equation which keeps the angular dependence of the backscattering function fully intact, are required to clarify the origin of the humps.

At this point, it is appropriate to comment on the preliminary results for Ag we included in a perspective paper about the electron microphysics at plasma-solid interfaces [58]. There, we claimed to reach good agreement between experimental and theoretical data by adjusting an energy-dependent electron-phonon coupling strength. Incoherent scattering on the ion cores was not considered, as was the scattering on surface defects. In addition, the surface potential was the exponential barrier employed by Roupie and coworkers [21]. The studies on which the present report is based revealed, however, that the exponential barrier is a bad approximation to the image step (irrespective of the numerical value of the additional adjustable parameter, which it brings in) and that the good adjustment disappears by incorporating the angular dependence of electron-phonon scattering. Since we now find fair agreement for a variety of metals, we consider the conclusions reached in this work as robust.

Finally, let us comment on the debate in the plasma physics community [35, 36] which arose around the initial measurements by Cimino and coworkers [5]. In particular, their claim that the yields reach unity for vanishing impact energy was critically seen. In the meantime, however, Cimino's group scrutinized the data very carefully [33, 34]; the work by Gonzalez and coworkers [34] is one of the follow-up investigations. Specifically in Ref. [33] they estimated the errors of their measurements at low energies, with the conclusion that an unanimous

claim for unit reflectivity at zero energy cannot be maintained. General arguments, and also the explicit calculation of MacColl [47], indeed show that unit reflectivity cannot occur on an image step. A Bragg gap, however, as we have seen above for the single-crystal Cu(100) surface, could lead to an increase of the reflectivity, and hence, the emission yield. We would in fact expect the same for single-crystal Au(100) and Ag(100) surfaces, since they have Bragg gaps around the vacuum level [57] (shaded regions in the middle and lower panels of Fig. 5), and would encourage measurements on them. For the polycrystalline Ag and Au samples used by Cimino's group, however, this cannot occur, supporting thus Andronov and coworkers' [35, 36] critique of Cimino and coworkers' initial interpretation of the measured data. An explanation of the discrepancies between the recent [34] and the previous [37] noble metal data remains however outside our approach. We cannot account for it by the surface scattering strength C . Most probably, its origin has to be sought in chemical modifications of the surface.

IV. CONCLUSION

We presented an equation for the secondary electron emission yield $Y(E, \xi)$, which combines the three stages of the process: transmission of a primary electron through the surface potential, scattering cascades inside the bulk of the solid exciting secondary electrons, and escape of secondaries by transmission through the surface potential in the reverse direction. The structure of the expression, resembling a conditional (pseudo-)probability in its central part, which is the escape function $\mathcal{E}(E, \xi)$, reflects the three stages in a rather transparent manner. Due to the explicit consideration of the transmission through the surface potential, the expression for $Y(E, \xi)$ is particularly suitable for describing secondary emission from surfaces at very low electron impact energies.

The two main building blocks of the formula for the escape function are the surface transmission function $D(E, \xi)$ and the backscattering function $Q(E\eta|E'\eta')$. The former, to be obtained from a quantum-mechanical calculation matching the states inside the solid to the ones outside of it, reflects the electronic structure of the surface, while the latter, obtained from the invariant embedding principle, contains the bulk scattering processes. To account for electron multiplication due to electron-electron scattering, the part of the backscattering function arising from it is normalized to two.

In this work, we calculated the surface transmission function for an image step, augmented by diffraction on crystal planes parallel to the surface and elastic scattering on surface defects. The backscattering function was obtained from an augmented effective mass model, including statically screened electron-electron scattering, electron-impurity scattering, quasi-elastic electron-phonon scattering, and incoherent scattering on the potentials of the ion cores, which turned out to be rather

important for getting a good match of calculated and measured yields. As a first step of solving the nonlinear embedding equation for $Q(E\eta|E'\eta')$, we decoupled angular and energy integrations by the quasi-isotropic approximation.

Despite the simplicity of the model and the crudeness of the quasi-isotropic approximation, calculated and measured data are rather close to each other, indicating the calculational scheme captures the essentials of secondary emission from metal surfaces at very low electron impact energies. The discrepancies between theory and measurements which remain could be due to shortcomings of the quasi-isotropic approximation, which assumes isotropy of electron backscattering irrespective of the energy transfer, while it is actually only the case for elastic processes, or the limitations of the effective two-band model used to obtain the surface transmission function $D(E, \xi)$. In principle, the lack of dynamic screening and the lack of the bulk crystal structure in the transition rates could be further causes. But we do not expect it to be critical. From our perspective, the next step should be to calculate $Q(E\eta|E'\eta')$ without the quasi-isotropic approximation. Combined with the expression for the emission yield we have given in this work, one would then have a powerful alternative to Monte-Carlo simulations of secondary electron emission at low impact energies.

ACKNOWLEDGMENTS

We thank Kristopher Rasek from the University Greifswald for critical reading of the manuscript. F.X.B. thanks Igor Kaganovich from the Princeton Plasma Physics Laboratory for discussions and help with the Russian literature.

Appendix A: Quasi-isotropic approximation

The goal of the quasi-isotropic approximation is to decouple the energy from the angular variables and to reduce thereby the embedding equation, which is a four-dimensional integral equation, to a two-dimensional one.

The embedding equation, as it arises from the invariant embedding principle for electron backscattering [24], can be written as

$$Q = K^- + K_1^+ \circ Q + Q \circ K_2^+ + Q \circ B^- \circ Q \quad (\text{A1})$$

where the \circ operation is defined by

$$(A \circ B)(E\eta|E'\eta') = \int_{E'}^E dE'' \int_{\eta_c}^1 d\eta'' A(E\eta|E''\eta'') \times B(E''\eta''|E'\eta'), \quad (\text{A2})$$

and a cut-off $\eta_c = 10^{-4}$ is introduced to exclude extreme grazing entrance and exit angles, which are hardly realized experimentally, but would require the handling of

integrable singularities, making the numerics thus unnecessarily involved.

The kernels of (A1) are given by

$$K^-(E\eta|E'\eta') = \frac{G^-(E\eta|E'\eta')}{H(E\eta|E'\eta')}, \quad (\text{A3})$$

$$K_1^+(E\eta|E''\eta''; E'\eta') = \frac{G^+(E\eta|E''\eta'')\rho(E'')}{H(E\eta|E'\eta')}, \quad (\text{A4})$$

$$K_2^+(E''\eta''|E'\eta'; E\eta) = \frac{\rho(E'')G^+(E''\eta''|E'\eta')}{H(E\eta|E'\eta')}, \quad (\text{A5})$$

$$B^-(E''\eta''|E'''\eta'''; E\eta E'\eta') = \frac{\rho(E'')G^-(E''\eta''|E'''\eta''')\rho(E''')}{H(E\eta|E'\eta')} \quad (\text{A6})$$

with

$$G^\pm(E\eta|E'\eta') = \sum_{i=ee,el} \frac{W_i^\pm(E\eta|E'\eta')}{v(E)\eta} \quad (\text{A7})$$

the transition rate per length, obtained from the individual transition rates per time $W_i^\pm(E\eta|E'\eta')$, where $i = ee, ei$, presented in Section II C. The function

$$H(E\eta|E'\eta') = \frac{\gamma(E)}{v(E)\eta} + \frac{\gamma(E')}{v(E')\eta'}, \quad (\text{A8})$$

usually written on the left side of (A1), denotes the total rate per length that the impinging electron scatters in the infinitesimally thin additional material layer envisaged in the embedding principle. It is given in terms of the electron velocity $v(E) = 2\sqrt{E+U}$ and the total scattering rate per time,

$$\gamma(E) = \sum_{i=ee,el} C_i \int_{-\Phi}^E dE' \int_0^1 d\eta' \rho(E') \left[W_i^+(E\eta|E'\eta') + W_i^-(E\eta|E'\eta') \right], \quad (\text{A9})$$

which in fact is independent of η . The factor $C_{ee} = 1/2$ avoids double counting of the final states in an electron-electron scattering event [17] and $C_{el} = 1$.

The reasoning behind the quasi-isotropic approximation is that backward scattering, encoded in K^- , depends only weakly on the angular variables. It simplifies the embedding equation (A1) significantly, since it provides the freedom to fix on the rhs, under the integrals over the direction cosines, the angular dependencies of the backscattering functions to the ones of the backscattering function on the lhs. This opens up the possibility to solve (8) iteratively by an expansion in the number of backscattering events (all with the same values for η and η') which encounters in each iteration step just a linear integral equation in two energy variables.

Before discussing how valid the quasi-isotropic approximation in fact is, let us state the kernels to which it leads. Utilizing it turns η and η' to external variables. Equation (A1) reduces then to (8) given in Section II B with

$$K_1^+(E|E''; E'\eta\eta') = \int_{\eta_c}^1 d\eta'' K_1^+(E\eta|E''\eta''; E'\eta'), \quad (\text{A10})$$

$$K_2^+(E''|E'; E\eta\eta') = \int_{\eta_c}^1 d\eta'' K_2^+(E''\eta''|E'\eta'; E\eta), \quad (\text{A11})$$

and

$$B^-(E''|E'''; E\eta E'\eta') = \int_{\eta_c}^1 d\eta'' \int_{\eta_c}^1 d\eta''' B^-(E''\eta''|E'''\eta'''; E\eta E'\eta'). \quad (\text{A12})$$

Let us now address the validity of the quasi-isotropic approximation. The angular dependence of K^- decides whether it is justified or not. To be valid, it should be nearly isotropic because, in leading order, Eq. (A1) suggests $Q = K^-$. Hence, provided K^- has a weak angular dependence, so will Q . By anticipating this, we can thus move in the three integral terms of (A1) the backscattering functions Q in front of the angular integrals and set the direction cosines of the Q 's to η and η' , in the manner indicated above, that is, to the direction cosines on which the inhomogeneity K^- and the Q on the lhs depend.

A representative angular dependence of $K^-(E\eta|E'\eta')$ is plotted in Fig. 6, using the model described in Section II C and material parameters for Al. Starting with elastic scattering in the upper left and moving clockwise through the plots, data are shown for increasing energy transfer. Clearly, elastic backscattering is rather isotropic. The quasi-isotropic approximation is well justified for it. For finite energy transfer, however, that is, for inelastic backscattering due to electron-electron collisions, isotropy is no longer strictly given, especially, for large direction cosines, where the Pauli principle excludes final states. The quasi-isotropic approximation neglects this and assumes, irrespective of the energy transfer, $K^-(E\eta|E'\eta')$ to be a weakly varying function of its angular variables. Since the reduction of computational costs is large and the agreement between calculated and measured yields is rather good, we consider the approximation as a viable first step towards a complete solution of the embedding equation, which then, of course, has to keep energy and angular variables fully intact.

Appendix B: Solution of Eq. (8)

In this appendix, we describe the strategy we employed for solving the embedding equation in the quasi-isotropic approximation. To grasp the algebraic structure of the approach, we suppress in the following the independent

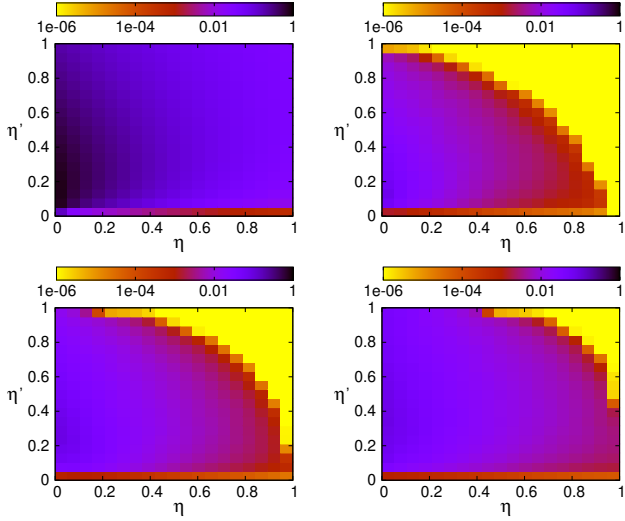


FIG. 6. (color online) Angular dependence of $K^-(E\eta|E'\eta')$ for Al using the model described in Section II C. From the upper left moving clockwise through the plots, the initial energy $E = 17.45$ eV, while the final energies are $E' = 17.45, 12.34, 7.24,$ and 2.13 eV. The nonmonotonous growth of the Pauli-blocked zone with energy transfer (yellow regions) is due to the denominator $\eta v(E)H(E\eta|E'\eta')$ in the definition (A3) of K^- . Angular resolution is the one taken for the numerical solution of Eq. (8) sketched in Appendix B.

variables and adopt a symbolic notation, in which the separation (9) simply reads

$$A = A_{ee} + A_{el}\delta(E - E'). \quad (\text{B1})$$

Using the splitting for the functions entering (8), collecting all terms proportional to $\delta(E - E')$, and forcing them to vanish yields an algebraic equation for Q_{el} and an integral equation for Q_{ee} . The algebraic structure of the two equations is identical. In an abstract notation, they both can be cast into the form

$$Q_i = K_i^- + K_{1,i}^+ Q_i + Q_i K_{2,i}^+ + Q_i B_i^- Q_i. \quad (\text{B2})$$

with $i = el, ee$. For $i = el$ the kernels are just the factors in K^- and $K_{1,2}^+$ which are in front of $\delta(E - E')$, while for $i = ee$ the kernels are renormalized and given by

$$K_{ee}^- \rightarrow \tilde{K}_{ee}^- = \frac{N^-}{D}, \quad K_{1,ee}^+ \rightarrow \tilde{K}_{1,ee}^+ = \frac{N_1^+}{D}, \quad (\text{B3})$$

$$K_{2,ee}^- \rightarrow \tilde{K}_{2,ee}^- = \frac{N_2^+}{D}, \quad B_{ee}^- \rightarrow \tilde{B}_{ee}^- = \frac{B_{ee}^-}{D} \quad (\text{B4})$$

with

$$D = 1 - K_{1,el}^+ - K_{2,el}^+ - Q_{el}B_{el}^- - B_{el}^-Q_{el}, \quad (\text{B5})$$

$$N^- = K_{ee}^- + Q_{el}B_{ee}^-Q_{el} + K_{1,ee}^+Q_{el} + Q_{ee}K_{2,ee}^+, \quad (\text{B6})$$

$$N_1^+ = K_{1,ee}^+ + Q_{el}B_{ee}^-, \quad (\text{B7})$$

$$N_2^+ = K_{2,ee}^+ + B_{ee}^-Q_{el} \quad (\text{B8})$$

and the energy variables of the (one-energy) functions Q_{el} such that they coincide, depending on the relative ordering, with the left or right energy variables of the (two-energy) functions next to them.

The algebraic equation for Q_{el} is readily solved. Defining an auxiliary function

$$Q_{el}^{(1)} = \frac{K_{el}^-}{1 - K_{1,el}^+ - K_{2,el}^+} \quad (\text{B9})$$

one obtains

$$Q_{el} = \frac{K_{el}^-}{2B_{el}^-Q_{el}^{(1)}} \left[1 - \sqrt{1 - \frac{4B_{el}^- (Q_{el}^{(1)})^2}{K_{el}^-}} \right], \quad (\text{B10})$$

provided $D = 1 - 4B_{el}^- (Q_{el}^{(1)})^2 / K_{el}^- \geq 0$, otherwise $Q_{el} = Q_{el}^{(1)}$. The dependence of the functions in (B10) on E, η and η' is easily restored by looking at (9).

To solve the integral equation for Q_{ee} , we employ an iterative approach. It expands Q_{ee} in powers of \tilde{K}_{ee}^- , that is, in the number of renormalized backscattering events, as given in Eq. (10). The expansion coefficients satisfy a set of linear integral equations. Writing out the dependencies on energies and direction cosines explicitly, the equations read

$$Q_{ee}^{(n)}(E|E'; \eta\eta') = \tilde{K}_{ee}^{(n),-}(E|E'; \eta\eta') + \int_{E'}^E dE'' \tilde{K}_{1,ee}^+(E|E''; E'\eta\eta') Q_{ee}^{(n)}(E''|E'; \eta\eta') + \int_{E'}^E dE'' Q_{ee}^{(n)}(E|E''; \eta\eta') \tilde{K}_{2,ee}^+(E''|E'; E\eta\eta'), \quad n = 1, 3, \dots, n_{\max} \quad (\text{B11})$$

with

$$\tilde{K}_{ee}^{(2l+1),-}(E|E'; \eta\eta') = \sum_{k=0}^{l-1} \int_{E'}^E dE'' \int_{E'}^{E''} dE''' Q_{ee}^{(2k+1)}(E|E''; \eta\eta') \tilde{B}_{ee}^-(E''|E'''; E'E'\eta\eta') Q_{ee}^{(2(l-k)-1)}(E'''|E'; \eta\eta') \quad (\text{B12})$$

for $l \geq 1$ and $\tilde{K}_{ee}^{(1),-} = \tilde{K}_{ee}^-$. By construction, the max-

imum number of backscattering events n_{\max} is always

odd. Due to the Volterra-type structure of the energy integrals, Eq. (B11) can be discretized in such a way that the $Q_{\text{el}}^{(k)}$ appearing in the inhomogeneity $\tilde{K}_{\text{ee}}^{(2l+1),-}$ are known from the previous steps of the calculation. We obtained convergence by iterating up to $n_{\text{max}} = 13$.

In the numerical implementation we set an energy cut-off $E_{\text{max}} = 20 \text{ eV}$ and discretized the energy interval $[-\Phi, E_{\text{max}}]$ by $N = 20$ slices. The interval of the internal direction cosines, $[\eta_{\text{min}}, 1]$, is also split into $M = 20$ subintervals. Thus, after discretization, Eq. (B11) is, for each iteration step, a linear algebraic equation on a $N \times N$ energy grid, which has to be solved for each doublet (η, η') drawn from the $M \times M$ angular grid. For the chosen discretization, the resolution in energy $\Delta E \approx 0.7 \text{ eV}$, while the resolution in direction cosine $\Delta \eta \approx 0.05$. The integrals of the escape function (2) are calculated on the same grids, truncated, however, by the lower bounds $\eta_{\text{min}}(E)$ and $E_{\text{min}}(\eta')$, whereas the integrals required for γ , K_1^+ , K_2^+ , and B^- (cf. Eqs. (A9)–(A12)) are done by Gaussian integrations. For imperfect surfaces, finally, integrations over the external direction cosine ξ are required, which again are discretized by 20 slices. Numerically most expensive is the Monte-Carlo integration required for the electron-electron transition rate. The other parts of the code perform rather efficiently by taking advantage of the multicore structure of modern processors.

Appendix C: Electron-electron transition rate

The complete electron-electron transition rate, including direct and exchange scattering, on which the calculation of the emission yield is based, is given in this appendix. The manipulations presented below can be made for a dynamically screened Coulomb interaction $U(q, \omega) = 1/q^2 \varepsilon(q, \omega)$, but we give the result only for a statically screened Coulomb potential,

$$U(q) = V(q, 0) = \frac{1}{q^2 + \kappa^2}, \quad (\text{C1})$$

because this is the one we considered in the calculation of the emission yield (cf. Eq. (17)).

The starting point is the expression for the transition rate due to electron-electron scattering [59],

$$\begin{aligned} W_{\text{ee}}(\vec{k}|\vec{k}') &= \frac{2}{\pi^3} \int d^3q d^3q' n_{\text{F}}(E_q) \bar{n}_{\text{F}}(E_{q'}) \\ &\times |M(\vec{k}\vec{q}|\vec{k}'\vec{q}')|^2 \delta(E_k + E_q - E_{k'} - E_{q'}) \\ &\times \delta(\vec{k} + \vec{q} - \vec{k}' - \vec{q}'), \end{aligned} \quad (\text{C2})$$

with \vec{k} and \vec{k}' the momenta of the electron in the initial and final state, $\bar{n}_{\text{F}}(E_q) = 1 - n_{\text{F}}(E_q)$, where $n_{\text{F}}(E_q)$ is the

Fermi function, and $M(\vec{k}\vec{q}|\vec{k}'\vec{q}')$ the sum of the three matrix elements corresponding to the three Coulomb terms diagrammatically shown in Fig. 1c. Energies are measured from the bottom of the conduction band. Hence, for an effective electron mass equal to the bare electron mass, the situation to which we restrict our considerations, as mentioned in the main text, $E_k = k^2$ with $k = |\vec{k}|$ and similarly for the other energies. For the electrons of the Fermi sea, both spin orientations are taken into account.

The task is to express, after \vec{q}' is integrated out, the remaining momenta (\vec{k} , \vec{k}' and \vec{q}) in terms of total energies (E , E' , and \tilde{E}), direction cosines (η , η' , and $\tilde{\eta}$), and azimuth angles (ϕ_k , $\phi_{k'}$, and ϕ_q). Distinguishing forward and backward scattering with respect to the surface normal and integrating out the azimuth angles yields then the transition rate $W_{\text{ee}}^{\pm}(E\eta|E'\eta')$ needed for the kernels of the embedding equation and the calculation of $\gamma(E)$. In the following, the labels p , p' , and \tilde{p} denote, respectively, the sign of the z-components of the vectors \vec{k} , \vec{k}' and \vec{q} , while the variables T , T' and \tilde{T} stand for the lateral energies associated with them. For instance, $T = (E + U)(1 - \eta^2)$ and likewise for the other combinations. The lateral energies can thus be used as alternatives to the direction cosines. In terms of the functions which follow,

$$W_{\text{ee}}^{\pm}(E\eta|E'\eta') = W_{\text{ee}}(ETp = 1|E'T'p' = \pm 1), \quad (\text{C3})$$

while the momentum transfer $g^{\pm}(E\eta|E'\eta'; \phi)$ employed in Eqs. (15) and (18) becomes

$$g^{\pm}(E\eta|E'\eta'; \phi) = \tilde{g}(ETp = 1|E'T'p' = \pm 1; \phi). \quad (\text{C4})$$

Using the homogeneity in the lateral directions to measure the azimuth angles with respect to the projection of one of the momenta onto the xy -plane, for instance, the projection of the vector \vec{k} , and defining

$$R_1 = |\vec{k} - \vec{k}'|_{pp'} = \tilde{g}(ETp|E'T'p'; \phi_{k'}), \quad (\text{C5})$$

$$R_2 = |\vec{q} - \vec{k}'|_{\tilde{p}p'} = \tilde{g}(\tilde{E}\tilde{T}\tilde{p}|E'T'p'; \phi_q - \phi_{k'}), \quad (\text{C6})$$

where

$$\begin{aligned} \tilde{g}(ETp|E'T'p'; \phi) &= (T + T' - 2\sqrt{TT'} \cos \phi \\ &- [p\sqrt{E + U - T} - p'\sqrt{E' + U - T'}]^2)^{1/2}, \end{aligned} \quad (\text{C7})$$

yields, after setting $\tilde{E} = E_q - U = \tilde{T} + \tilde{q}^2 - U$ and working out the energy-conserving δ -function,

$$W_{ee}(ETp|E'T'p') = \sum_{\tilde{p}=\pm 1} \int_0^\infty d\tilde{T} \int_0^{2\pi} d\phi_{k'} \int_0^{2\pi} d\phi_q \frac{U(R_1, R_2)N(E, E', \tilde{E})}{|r(ETp|E'T'p')|} \Theta(\tilde{q}(ETp|E'T'p'; \tilde{p}\tilde{T}\phi_{k'}\phi_q)) \quad (\text{C8})$$

with $\Theta(x) = 1$ for $x \geq 1$ and zero otherwise,

$$U(R_1, R_2) = 2([U(R_1)]^2 + [U(R_2)]^2 - U(R_1)U(R_2)) , \quad (\text{C9})$$

$$N(E, E', \tilde{E}) = \pi^{-3} n_F(\tilde{E} + U) \bar{n}_F(E - E' + \tilde{E} + U) , \quad (\text{C10})$$

$$\tilde{q}(ETp|E'T'p'; \tilde{p}\tilde{T}\phi_{k'}\phi_q) = \frac{s(ETp|E'T'p'; \phi_{k'}) - h(TT'; \phi_q, \phi_q - \phi_{k'})\sqrt{\tilde{T}}}{\tilde{p}r(ETp|E'T'p')} , \quad (\text{C11})$$

where

$$s(ETp|E'T'p'; \phi_{k'}) = E - E' - [\tilde{g}(ETp|E'T'p'; \phi_{k'})]^2 , \quad (\text{C12})$$

$$h(TT'; \phi_q, \phi_q - \phi_{k'}) = 2(\sqrt{\tilde{T}} \cos \phi_q - \sqrt{\tilde{T}'} \cos(\phi_q - \phi_{k'})) , \quad (\text{C13})$$

$$r(ETp|E'T'p') = 2(p\sqrt{E + U - \tilde{T}} - p'\sqrt{E' + U - \tilde{T}'}) . \quad (\text{C14})$$

Although the expression for W_{ee} is perhaps somewhat involved, it follows straight from energy conservation, which after \tilde{q}' is integrated out is encoded in $\delta(E_k + E_q - E_{k'} - E_{|\tilde{k}+\tilde{q}-\tilde{k}'|})$. In terms of our variables, and suppressing all dependencies except the one on \tilde{E} , this becomes $\delta(f(\tilde{E}))$ with $f(\tilde{E}) = s - h\sqrt{\tilde{T}} - \tilde{p}r\sqrt{E - \tilde{T} + U}$. Integrating over \tilde{E} and renaming the solution \tilde{E}_0 of $f(\tilde{E}_0) = 0$ by \tilde{E} yields, after taking the Jacobi determinant of the variable transformation into account, Eq. (C8).

The remaining three integrals cannot be done analytically. We employed for it a Monte-Carlo integrator. Had we considered only the direct terms, a different strategy, based on rewriting the energy-conserving δ -function in terms of an integral over a product of two δ -functions, could have been employed, leading to $W_{ee}^\pm|_D$ given in Eq. (18). In the notation of this appendix, the $W_{ee}^\pm|_D$ arises from the $[U(R_1)]^2$ term in Eq. (C9). We verified that the result of the Monte-Carlo integration of this term alone coincides with the numerical result obtained directly from Eq. (18).

-
- [1] A. J. Dekker, in *Solid State Physics*, edited by F. Seitz and D. Turnbull (Academic Press, New York, 1958), p. 251.
- [2] F. Salvat-Pujol and W. S. M. Werner, *Surf. Interface Anal.* **45**, 873 (2013).
- [3] J. Cazaux, *J. Appl. Phys.* **111**, 064903 (2012).
- [4] A. Klassen, A. Bauereiss, and C. Koerner, *J. Phys. D: Appl. Phys.* **47**, 065307 (2014).
- [5] R. Cimino, I. R. Collins, M. A. Furman, M. Pivi, F. Ruggerio, G. Rumolo, and F. Zimmermann, *Phys. Rev. Lett.* **93**, 014801 (2004).
- [6] P. Tolias, M. Komm, S. Ratynskaia, and A. Podolnik, *Nucl. Mat. and Energy* **25**, 100818 (2020).
- [7] L. Vignitchouk, G. L. Delzanno, P. Tolias, and S. Ratynskaia, *Phys. Plasmas* **25**, 063702 (2018).
- [8] M. D. Campanell and M. V. Umansky, *Phys. Rev. Lett.* **116**, 085003 (2016).
- [9] P. Tolias, *Plasma Phys. Control. Fusion* **56**, 123002 (2014).
- [10] P. Tolias, *Plasma Phys. Control. Fusion* **56**, 045003 (2014).
- [11] J. Choi, F. Iza, J. K. Lee, and C.-M. Ryu, *IEEE Transactions on Plasma Science* **35**, 1274 (2007).
- [12] Y. Raitses, D. Staack, M. Keidar, and N. J. Fisch, *Phys. Plasma* **12**, 057104 (2005).
- [13] F. Taccogna, S. Longo, and M. Capitelli, *Phys. Plasma* **11**, 1220 (2004).
- [14] A. Bellissimo, G. M. Pierantozzi, A. Ruocco, G. Stefani, O. Y. Ridzel, V. Astašauskas, W. S. M. Werner, and M. Taborrelli, *J. Electron Spectros. Relat. Phenom.* **241**, 146883 (2020).
- [15] C. G. H. Walker, M. M. El-Gomati, A. M. D. Assa'd, and M. Zdražil, *Scanning* **30**, 365 (2008).
- [16] P. A. Wolff, *Phys. Rev.* **95**, 56 (1954).
- [17] D. R. Penn, S. P. Apell, and S. M. Girvin, *Phys. Rev. B* **32**, 7753 (1985).
- [18] M. Azzolini, M. Angelucci, R. Cimino, R. Larciprete, N. M. Pugno, S. Taioli, and M. Dapor, *J. Phys. Condens. Matter* **31**, 055901 (2019).
- [19] H.-Y. Chang, A. Alvarado, and J. Marian, *Appl. Surf. Sci.* **450**, 190 (2018).
- [20] J. Pierron, C. Inguibert, M. Belhaj, T. Gineste, J. Puech, and M. Raine, *J. Appl. Phys.* **121**, 215107 (2017).
- [21] J. Roupie, O. Jbara, T. Tondou, M. Belhaj, and J. Puech, *J. Phys. D: Appl. Phys.* **46**, 125306 (2013).
- [22] V. A. Ambartsumian, *Russ. Astronom. J.* **19**, 1 (1942).
- [23] S. Chandrasekhar, *Radiative Transfer* (Dover Books,

- New York, 1960).
- [24] R. Dashen, *Phys. Rev.* **134**, A1025 (1964).
- [25] M. Azzolini, O. Y. Ridzel, P. S. Kaplya, V. Afanas'ev, N. M. Pugno, S. Taioli, and M. Dapor, *Comp. Mat. Sci.* **173**, 109420 (2020).
- [26] C. Figueroa, H. Brizuela, and S. P. Heluani, *J. Appl. Phys.* **115**, 193703 (2014).
- [27] L. G. Glazov and I. Pázsit, *Nucl. Instr. and Meth. B* **256**, 638 (2007).
- [28] L. G. Glazov and S. Tougaard, *Phys. Rev. B* **68**, 155409 (2003).
- [29] M. Vicanek, *Surf. Sci.* **440**, 1 (1999).
- [30] V. P. Afanas'ev and S. V. Pavlenko, *Z. Phys. B* **93**, 357 (1994).
- [31] F. X. Bronold and H. Fehske, *Phys. Rev. Lett.* **115**, 225001 (2015).
- [32] F. X. Bronold and H. Fehske, *Plasma Phys. Control. Fusion* **59**, 014011 (2017).
- [33] R. Cimino, L. A. Gonzalez, R. Larciprete, A. Di Gaspare, G. Iadarola, and G. Rumolo, *Phys. Rev. Spec. Topics* **18**, 051002 (2015).
- [34] L. A. Gonzalez, M. Angelucci, R. Larciprete, and R. Cimino, *AIP Advances* **7**, 115203 (2017).
- [35] A. N. Andronov, A. S. Smirnov, I. D. Kaganovich, E. A. Startsev, Y. Raitses, and V. I. Demidov, Report No. CERN-2013-002 p. 161 (2013).
- [36] A. N. Andronov, St. Petersburg State Polytechnical University *J. Phys. Math.* p. 67 (2014).
- [37] I. M. Bronshtein and V. V. Roshchin, *Sov. J. Tech.-Phys.* **3**, 2271 (1958).
- [38] E. G. McRae and C. W. Caldwell, *Surf. Sci.* **57**, 77 (1976).
- [39] Z. Yakubova and N. A. Gorbatyi, *Izv. VUZ. Fiz.* **7**, 129 (1972).
- [40] Z. Yakubova and N. A. Gorbatyi, *Izv. VUZ. Fiz.* **11**, 88 (1970).
- [41] I. M. Bronshtein and B. C. Fraiman, *Secondary Electron Emission* (Nauka, Moscow, 1969).
- [42] I. H. Khan, J. P. Hobson, and R. A. Armstrong, *Phys. Rev.* **129**, 1513 (1963).
- [43] E. Bauer, *J. Vac. Sci. Technol.* **7**, 3 (1970).
- [44] D. L. Smith, E. Y. Lee, and V. Narayanamurti, *Phys. Rev. Lett.* **80**, 2433 (1998).
- [45] W. S. M. Werner, I. S. Tilinin, and M. Hayek, *Phys. Rev. B* **50**, 4819 (1994).
- [46] N. Garcia and J. Solana, *Physica* **81 B**, 296 (1976).
- [47] L. A. MacColl, *Phys. Rev.* **56**, 699 (1939).
- [48] P. Linz and T. C. Chen, *Int. J. Quant. Chemistry* **11**, 991 (1977).
- [49] E. Kieft and E. Bosch, *J. Phys. D: Appl. Phys.* **41**, 215310 (2008).
- [50] W. A. Harrison, *Phys. Rev.* **139**, A 179 (1965).
- [51] J. F. Thomas, Jr., *Phys. Rev. B* **7**, 2385 (1973).
- [52] B. P. Barua and S. K. Sinha, *J. Appl. Phys.* **49**, 3967 (1978).
- [53] N. W. Ashcroft and N. D. Mermin, *Solid State Physics* (CPS Publishing Asia, Hong Hong, 1988).
- [54] F. Ladstädter, U. Hohenester, P. Puschnig, and C. Ambrosch-Draxl, *Phys. Rev. B* **70**, 235125 (2004).
- [55] R. F. Willis, *Phys. Rev. Lett.* **34**, 670 (1975).
- [56] P. Tolias, arXiv:1601.02047v1 (2016).
- [57] E. V. Chulkov, V. M. Silkin, and P. M. Echenique, *Surf. Sci.* **437**, 330 (1999).
- [58] F. X. Bronold, K. Rasek, and H. Fehske, *J. Appl. Phys.* **128**, 180908 (2020).
- [59] V. F. Gantmakher and Y. B. Levinson, *Carrier scattering in metals and semiconductors* (North-Holland, Amsterdam, 1987).